Chemical Engineering Journal 426 (2021) 131839

Contents lists available at ScienceDirect

Chemical Engineering Journal

journal homepage: www.elsevier.com/locate/cej

Construction of multifunctional linear polyphosphazene and molybdenum diselenide hybrids for efficient fire retardant and toughening epoxy resins

Yuling Xiao, Guangyong Jiang, Chao Ma, Xia Zhou, Chenyu Wang, Zhoumei Xu, Xiaowei Mu *, Lei Song *, Yuan Hu

State Key Laboratory of Fire Science, University of Science and Technology of China, Hefei 230026, China

ARTICLE INFO

Keywords:
LPP-$MoSe_2$
Epoxy resin
Flame retardancy
Toughening

ABSTRACT

Epoxy resins (EP) are deemed as one kind of most commonly used thermosets, but immanently suffer from inflammability and brittleness. Herein, we report a newly designed hierarchical molybdenum diselenide ($MoSe_2$) nanotubes assembled from several-layered nanosheets, and then merged with linear polyphosphazene (LPP) for constructing LPP-$MoSe_2$ hybrids. LPP-$MoSe_2$ possesses great advantages in improving the properties of EP for their typical nanotube structure and the combination effect of transition metal, phosphorous and nitrogenous compounds. The developed EP/LPP-$MoSe_2$ composites present obvious reduction in flammability, obtaining a high LOI value of 29% and reaching V-0 rating in UL-94 test. They also exhibit obvious reduction in the heat hazards of EP, such as peak heat release rate (39.0%) and total heat release (24.8%), as well as the toxicity hazards including total smoke production (31.3%) and the yields of CO and CO_2. Gas-phase and condensed-phase mechanism are elucidated to explain the contribution of LPP-$MoSe_2$ to the fire retardation of EP. Moreover, the addition of LPP-$MoSe_2$ can also obviously enhance the mechanical properties of EP. The impact strength of EP is only 9 kJ/m^2, while EP/LPP-$MoSe_2$ 3.0 can reach up to 14.2 kJ/m^2. Based on tensile test, the well-dispersed LPP-$MoSe_2$ also leads to significant elevation in tensile strength (74.6%) and elongation at break (100%) of EP. Our data demonstrate that LPP-$MoSe_2$ shows impressive performance in developing high-performance EP composites, thereby broadening the practical application of EP.

1. Introduction

Nowadays, transition metal dichalcogenides (TMDs) featuring graphene-like layered architecture have received immense attention for its prominent physical properties and low cost [1,2]. Several classes of TMDs (MX_2) mainly consist of chalcogen (X: Se, S) and metal (M: Mo, W) through covalent bonds to form 2D monolayers (X-M−X) [3]. TMDs enable stacking of monolayers into a pre-designable layered structure through van der Waals interactions [4,5]. Various approaches similar to the preparation of graphene have been explored to fabricate 2D TMDs, mainly including liquid-phase exfoliation, mechanical exfoliation, electrochemical exfoliation, chemical vapor deposition, hydrothermal method, etc [6–8]. Most of the previous work laid the foundation for designing TMDs as high-performance nanoelectronics and optoelectronics with unique functions, such as photodetectors, transistors and light-emittng devices [9–11]. However, with the exception of molybdenum disulfide (MoS_2), exploration of TMDs in flame retardant fields remains largely unexplored.

As a burgeoning class of TMDs, molybdenum diselenide ($MoSe_2$) is of great significance for its exclusive properties than graphene [12]. The metallic nature of $MoSe_2$ renders them attractive as active catalysts, which also gives them potential as flame retardant additives to promote carbonization of polymers [13,14]. Wang et al., employed organic functionalized $MoSe_2$ sheets to enhance the fire safety of thermoplastic polyurethane, but the synthesis and application of $MoSe_2$ with hierarchical architecture were not attempted [15]. Specifically, a series of studies have found a strong mechanical strengthening effect toward polymer for flame retardants with nanotube structure [16,17]. Hence, it is intriguing to develop hierarchical $MoSe_2$ nanotubes for flame retardant and mechanical strengthening, simultaneously.

Polyphosphazenes have emerged as organic–inorganic hybrid polymers with an alternating phosphorus-nitrogen backbone and two organic side groups linked to phosphorus atoms, combining the properties of inorganic and organic polymers [18,19]. There are several types

* Corresponding authors.
E-mail addresses: xwmu@ustc.edu.cn (X. Mu), leisong@ustc.edu.cn (L. Song).

https://doi.org/10.1016/j.cej.2021.131839
Received 25 May 2021; Received in revised form 5 August 2021; Accepted 11 August 2021
Available online 17 August 2021

of polyphosphazenes with linear, cyclic, dendritic or cross-linked architecture, etc [20]. Thereinto, linear polyphosphazenes (LPPs) present one of the fastest growing polyphosphazenes since the stable and soluble polyphosphazene was first reported in the 1960 s [21]. The backbone of LPPs is featured with good flexibility, high thermal and optical stability, intrinsic fire resistance and good biological characteristics [22]. Insertion of various substituents (alkoxides, aryl oxides or amines) into phosphorus atoms via nucleophilic substitution between linear polydichlorophosphazene and nucleophiles can signally alter its chemical, physical and biological properties [23]. Many previous investigations have focused on fire retardant and self-extinguishing materials not only for its inorganic backbone with high phosphorus and nitrogen content but also for its high thermal stability [24–27]. However, the combination of LPPs with nanofiller was rarely attempted. With their good fire resistence and highly reactive phosphorus-chlorine bonds, the LPPs intrigue us to further investegate the linear polyphosphazene (LPP) / $MoSe_2$ hybrids for flame retardant applications.

Epoxy resins (EP) are considered as a sort of highly attractive thermosets with excellent properties (adhesive, corrosion resistance, easy manufacture, chemical and dimensional stability, etc.) and widespread applications (aerospace, electronics and transportation, etc.) [28]. As a huge threat to public life and property security, the enormous fire hazards (heat, smoke and toxic gases) of EP have become a stumbling block to its development [29,30]. Adhering to the concept of halogen-free, phosphorus- / silicon-containing flame retardants and nano-fillers are attracting considerable attention for designing EP with expected flame retardancy [31]. These flame-retardant additives have also raised grave concern regarding the impact on mechanical performance of EP. Furthermore, the commonest EP with plentiful aromatic ring structure usually have unsatisfied toughness for practical application because of their high crosslinking density and internal stress [32]. Great efforts in improving the toughness of EP have been made through loading nanoparticles or elastomers [33]. It is therefore practicable to design effective additives, which guarantee the comprehensively enhancement of flame retardancy and mechanical performances, especially fracture toughness.

Based on above descriptions, it is desirable to rationally design LPP / $MoSe_2$ hybrids for the flame retardancy and reinforcement of EP thermosets. Herein, we report a solvothermal synthesis of hierarchical $MoSe_2$ nanotubes assembled from several-layered nanosheets. The formation of hierarchical nanotubes can be divided into three stages: (1) the growth of $MoSe_2$ nanosheets; (2) the aggregation of $MoSe_2$ nanosheets into nanorods arising from the oriented attachment; (3) the construction of hollow nanotubes generated by Ostwald ripening effect [34]. The obtained nanotubes were treated by silane coupling agent (APTES) to obtain $–NH_2$ groups on its surface, which contributes to post-modification. Afterwards, linear polydichlorophosphazene synthesized by one-pot opproach with relatively high yield was applied to modify the surface and interface of the $MoSe_2$ nanosheets via nucleophilic substitution. In response to the flammability and poor toughness of epoxy resin (EP), the newly designed hybrids were introduced into EP nanocomposites. The thermal, fireproofing and mechanical performances of EP nanocomposites were studied. The strategies for the preparation of LPP / $MoSe_2$ hybrids and EP nanocomposites are displayed in Scheme 1.

2. Experimental section

2.1. Preparation of $MoSe_2$ nanotubes

As illustrated in Scheme 1, the hollow $MoSe_2$ nanotubes were synthesized via a solvothermal method. Briefly, 0.72 g of MoO_3 and 1.1 g of SeO_2 were dispersed in the mixture of octylamine (150 mL) and ethanol (100 mL) accompanied by magnetic stirring for 10 min. Then the mixture was transferred into a Teflon-lined stainless-steel autoclave and maintained at 190 °C for 24 h. The obtained black product (Fig. S1) was washed with ethanol and deionized water for several times and then vacuum-dried.

2.2. Synthesis of linear polydichlorophosphazene

Linear polydichlorophosphazene is the reactive precursor of LPP, which was synthesized via a one-pot approach [35]. A 250 mL three-neck flask equipped with a condenser pipe connected with HCl absorption tail and a magnetic stir bar was successively charged with 0.1 g of NH_2SO_3H, 0.1 g of $CaSO_4·2H_2O$, 7.71 g of NH_4Cl, 30 g of PCl_5, 6 mg of activated carbon and 22 mL of 1,2,4-trichlorobenzene. Under the protection of nitrogen, the system was slowly heated to 190 °C with stirring and reacted for 3.5 h. After reaction finished, the resultants were quickly filtered while hot to remove residual ammonium chloride and other residues. The filtrate was repeatedly precipitated with excessive

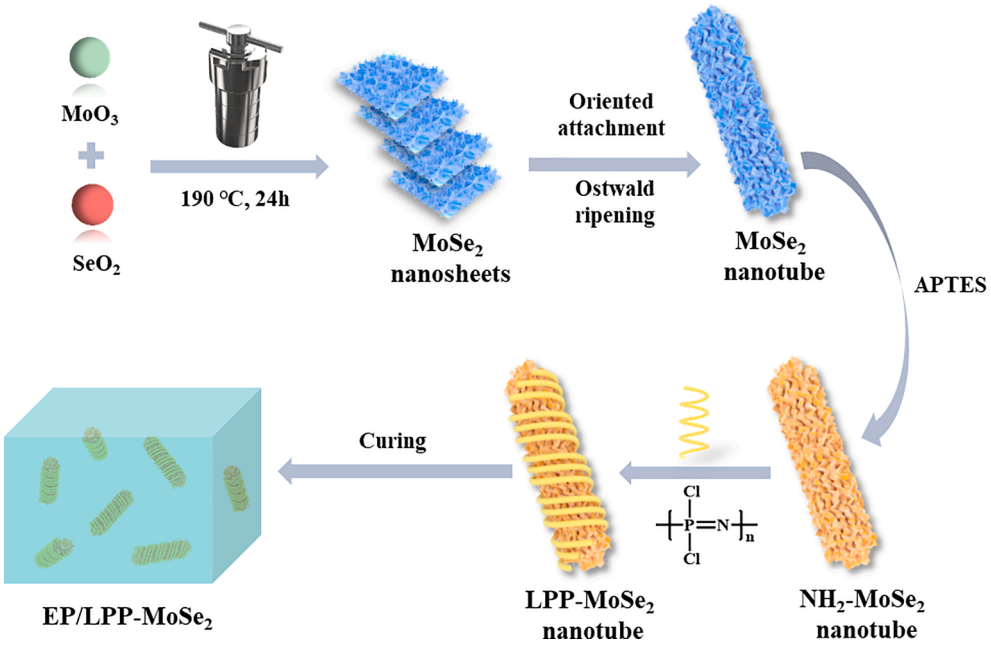

Scheme 1. Schematic illustration for the fabrication of the LPP-$MoSe_2$ nanotubes and its nanocomposites.

petroleum ether until the liquid is colorless and transparent. The precipitate was vacuum-dried at room temperature to give an off-white elastomer (6.65 g, yield 40%). ^{31}P NMR ($CDCl_3$): δ = -18.5 ppm. The molecular weight of linear polydichlorophosphazene was about 11000, with the polydispersity of 1.05.

2.3. Preparation of LPP modified $MoSe_2$ (LPP-$MoSe_2$)

The hollow $MoSe_2$ nanotubes were modified by 3-aminopropyltriethoxysilane (APTES) to obtain –NH_2 groups on the surface. Firstly, 2 g of $MoSe_2$ was homo-dispersed into ethanol aqueous containing 95 mL of ethanol and 5 mL of water under continuous stirring and ultrasonication for 3 h. Then 10 g of APTES was added under magnetic stirring and reacted at 50 °C for 12 h to achieve a hydrolysis reaction. The mixture was filtrated and washed with ethanol and deionized water for several times. The obtained product, abbreviated to NH_2-$MoSe_2$, was dried in an oven at 60 °C for 8 h. Subsequently, 2 g of NH_2-$MoSe_2$ after drying was homo-dispersed into 150 mL of tetrahydrofuran under continuous stirring and ultrasonication for 3 h. Then 12.8 g of triethylamine was added to the suspension. The linear polydichlorophosphazene was dissolved in dehydrated tetrahydrofuran and slowly dropped into the above system under the protection of nitrogen. After stirring at room temperature for 24 h, the mixture was filtered and washed with tetrahydrofuran, ethanol and deionized water for several times. The final product was dried in an oven at 60 °C for 8 h.

2.4. Fabrication of EP/LPP -$MoSe_2$ composites

The representative fabrication process of EP/2 wt% LPP-$MoSe_2$ composite is elaborated as follows: 1.1 g of LPP-$MoSe_2$ was homo-dispersed in 80 mL of acetone under ultrasonication and agitation for 1 h. Then 44.25 g of EP was added to the system followed by stirring and ultrasonication for another 2 h. The resulting homogeneous mixture was placed in a 100 °C oil bath to evaporate the acetone. Thereafter, the pre-melted 9.65 g DDM was mixed into it under stirring. The blending was poured into PTFE mould, pre-cured at 100 °C for 2 h and post-cured at 150 °C for another 2 h. The obtained EP composite containing 2 wt% LPP-$MoSe_2$ was labeled as EP/ LPP-$MoSe_2$ 2.0. The other EP composites were manufactured and denominated similarly.

All materials, instruments are supplied in the supplemental files.

3. Results and discussion

3.1. Characterization

A one-pot solvothermal method was employed to obtain hollow $MoSe_2$ nanotubes. The hollow $MoSe_2$ nanotubes modified by APTES contains plentiful amino groups that can easily interact with reactive chlorine atoms attached to the phosphorus atoms of linear polydichlorophosphazene through nucleophilic substitution, which makes them a novel hybrid hierarchical nanotubes (LPP-$MoSe_2$). The microstructures of $MoSe_2$ and LPP-$MoSe_2$ were confirmed by scanning electronic microscope (SEM). As shown in Fig. 1(a, c), the $MoSe_2$ exhibits a typical 1D rod-like structure with a wrinkled surface and the primary element components are Mo, Se and C. The structures indicated by arrows reveal that $MoSe_2$ are hollow nanotubes. As for LPP-$MoSe_2$ (Fig. 1 (b)), the original wrinkled surface disappears, and LPP is successfully anchored on the $MoSe_2$ surface to obtain a smoother surface. From the EDS-mapping results in Fig. 1(d), it is clear that P and N elements are detected and distributed on LPP-$MoSe_2$, verifying the successful attachment of LPP on $MoSe_2$. To further study the morphologies of the samples, the transmission electron microscopy (TEM) technique was performed and the results are exhibited in Fig. 2. The hierarchical $MoSe_2$ nanotubes with a diameter of about 320 nm have two closed tips and consist of several crimped nanosheets (Fig. 2(a, b)). As for LPP-$MoSe_2$, the $MoSe_2$ nanotubes are well-encapsulated by APTES and LPP with a thickness of about 180 nm, which leads to thicker LPP-$MoSe_2$ nanotubes (Fig. 2(c, d)).

The nitrogen adsorption–desorption isotherms and pore size distribution curves of $MoSe_2$ and LPP-$MoSe_2$ were measured at 77.4 K and illustrated in Fig. 3(a, b). Both $MoSe_2$ and LPP-$MoSe_2$ display a type-II adsorption isotherm [36]. The specific surface areas of $MoSe_2$ and LPP-$MoSe_2$ are 10.7 and 9.9 m^2/g, respectively. Additionally, the pore size distributions are mainly concentrated in the range of 3 ~ 4 nm with peaks around 3.5 nm, implying a mesoporous structure.

The structure information and chemical modification of $MoSe_2$

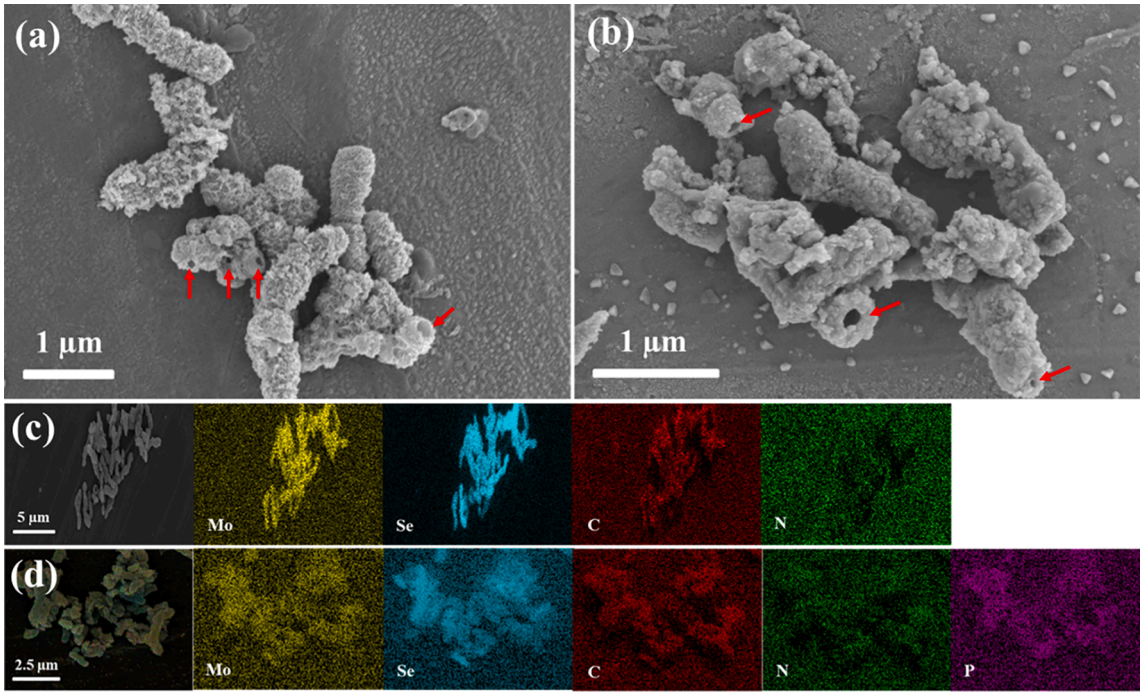

Fig. 1. SEM images and corresponding mapping results of the (a, c) $MoSe_2$ nanotubes and (b, d) LPP-$MoSe_2$ nanotubes.

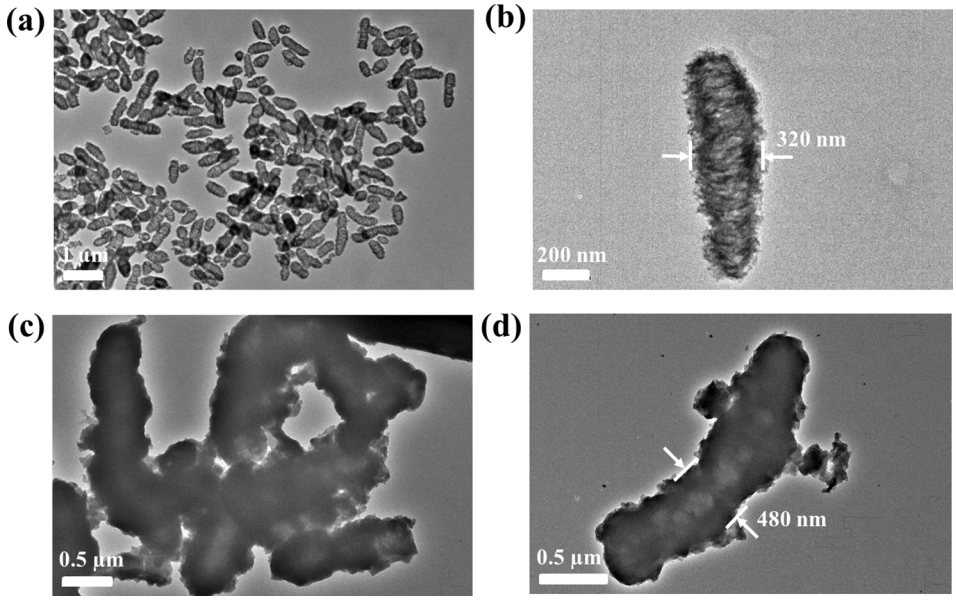

Fig. 2. TEM images of the (a-b) $MoSe_2$ nanotubes and (c-d) LPP-$MoSe_2$ nanotubes.

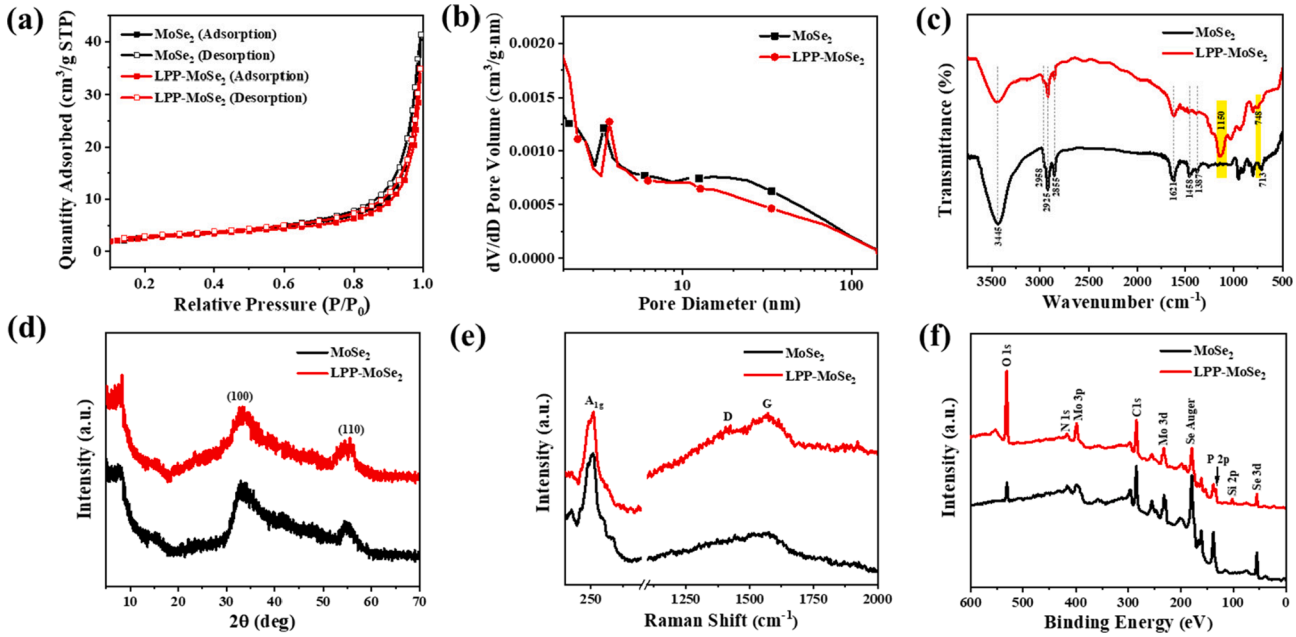

Fig. 3. (a) N_2 adsorption–desorption isotherms, (b) pore size distribution, (c) FT-IR, (d) XRD, (e) Raman and (f) XPS survey spectra $MoSe_2$ and LPP-$MoSe_2$ nanotubes.

nanotubes were investigated using fourier transform infrared spectrometer (FTIR) (Fig. 3(b)). In the spectrum of $MoSe_2$ nanotubes, the bands centered at 2958, 2925, 2855, 1458 and 1387 cm^{-1} correlate with the vibrations of $–CH_2$ and $–CH_3$. The band at 713 cm^{-1} implies the presence of $–(CH_2)_n$ ($n \geq 4$) chains [34]. The N–H group can be observed at 3445 and 1621 cm^{-1}, corresponding to the intercalated ammonia species and octylamine [37,38]. Meanwhile, the FTIR spectrum of NH_2-$MoSe_2$ is provided in Fig. S2 to characterize the grafting reaction of APTES on $MoSe_2$. The emerging peaks at 1100 and 808 cm^{-1} are attributed to the antisymmetric and symmetric stretching vibration of Si–O–Si, respectively [39]. In contrast with $MoSe_2$, the intensity ratio of N–H signal at 1616 cm^{-1} enhances, verifying the successful attachment of APTES on $MoSe_2$. After the further chemical modification with LPP, the P=N and P–N bonds in LPP chains appear at 1150 and 748 cm^{-1}, respectively, implying the formation of LPP-$MoSe_2$ [40,41].

Fig. 3(c) presents the X-ray diffraction (XRD) patterns of $MoSe_2$ and LPP-$MoSe_2$ with poor crystallinity. The characteristic peaks in $MoSe_2$ and LPP-$MoSe_2$ accord with the 2H-$MoSe_2$ phase (JCPDF 29–0914) [4]. Two broad diffraction peaks at 33° and 55° are attributed to the (1 0 0) and (1 1 0) planes of $MoSe_2$. There is no (0 0 2) plane reflection at 13.7°, which is ascribed to the altered normal (0 0 2) interlayer spacing of $MoSe_2$, implying the formation of few-layered $MoSe_2$. In Fig. 3(d), the Raman spectrum of the $MoSe_2$ nanotubes presents a characteristic peak at 249 cm^{-1}, which corresponds to the out-of-plane $A_{1g(Mo\text{-}Se)}$ mode [42,43]. In addition, two unconspicuous broad peaks near 1390 and 1560 cm^{-1} are also detected, associating with the disorder-induced D-band and the graphitic G-band of amorphous carbon, respectively [44,45]. The formation of amorphous carbon can be indexed to the carbonization of octylamine molecules during the solvothermal treatment. The above-mentioned characteristic peaks also exist in the Raman

spectrum of the LPP-$MoSe_2$ nanotubes, revealing that the original structure of $MoSe_2$ is retained after LPP encapsulation.

X-ray photoelectron spectroscopy (XPS) analysis was performed to provide crucial information with respect to chemical composition and valence state for $MoSe_2$ and LPP-$MoSe_2$. The survey spectrum of $MoSe_2$ exhibits that the surface elements of $MoSe_2$ are consist of Mo, Se, C, N, O (Fig. 3(e)). Moreover, an extra P element is clearly observed from the survey spectrum of LPP-$MoSe_2$. The detailed elementary composition information is recorded in Table S1 and the P content of LPP-$MoSe_2$ is 5.1%. The high-resolution XPS spectra of these samples are also provided in Fig. 4. In the Mo 3d spectrum of $MoSe_2$ (Fig. 4(a)), there is a pair of double peaks resolved into 1 T-$MoSe_2$ at the binding energy of 228.4 eV for Mo $3d_{5/2}$ and 231.5 eV for Mo $3d_{3/2}$ [1,46]. Another set of double peaks positioned at 229.6 eV for Mo $3d_{5/2}$ and 232.7 eV for Mo $3d_{3/2}$ reveals the formation of 2H-$MoSe_2$ [46,47]. From Fig. 4(b), the Se 3d spectrum of $MoSe_2$ exhibits similar two sets of bimodal peaks. Two peaks at 53.7 and 55.0 eV are affiliated to Se $3d_{5/2}$ and Se $3d_{3/2}$ of 1 T-$MoSe_2$, respectively, and two peaks at 54.7 and 55.7 eV are derived from Se $3d_{5/2}$ and Se $3d_{3/2}$ of 2H-$MoSe_2$, respectively [4,48,49]. These findings demonstrate that the prepared $MoSe_2$ consists of 1 T and 2H phase. Fig. 4 (c) shows the N 1s and Mo 3p signals of $MoSe_2$. The fitting peaks of N 1s are positioned at 398.7 and 401.4 eV, corresponding to N–C and $–NH_2$, respectively [50,51]. These signals are derived from the existence of N-doped amorphous carbon and contaminated octylamine in $MoSe_2$. After the modification, Si and P elements are observed, which originates from the introduction of APTES and LPP molecules, respectively. In Fig. 4(d), the Si 2p spectrum of LPP-$MoSe_2$ can be fitted with two peaks located at 102.2 and 103.2 eV, resulting from the Si–O–Si and Si–O–C bonds, respectively [52]. For the P 2p spectrum (Fig. 4(e)), the presence of P–NH–C and N–P=N signals at 133.8 and 137.8 eV, respectively, confirms that the LPP backbone is wrapped on the surface of $MoSe_2$ and the chlorine atoms of linear polydichlorophosphazene are substituted by amino groups. N 1 s and Mo 3p spectra of LPP-$MoSe_2$ exhibited in Fig. 4 (f) give further evidence of the modification. The detected P–NH–C (399.4) and N–P=N (398.9) signals well coincide with P 2p spectrum [25]. Specially, the original $–NH_2$ (401.4 eV) and Mo 3p (394.1 eV) are also exist with lower peak intensities, which is attributed to the substitution reaction and encapsulation of LPP. Based on above observations and analysis, the successful synthesis of $MoSe_2$ and further fabrication of LPP-$MoSe_2$ are thus evidenced.

Well dispersion effect of fillers is the prerequisite for the preparation of high-performance nanocomposites, especially high mechanical properties. It is hence imperative to observe the dispersion state of $MoSe_2$ and LPP-$MoSe_2$ in EP matrix. The ultrathin sections of EP composites were observed by TEM and the microstructures and dispersion status of additives are exhibited in Fig. 5. The $MoSe_2$ and LPP-$MoSe_2$ with original nanotube structure are observed in EP matrix. When the additive amount is below 2 wt%, both $MoSe_2$ and LPP-$MoSe_2$ show even distribution in the EP matrix without apparent agglomeration. With the addition of 3 wt%, only a small amount of aggregation of LPP-$MoSe_2$ occurs. The good compatibility may be ascribed to the presence of organic groups such as $–NH_2$ on the surface of fillers, which can enhance the interfacial interaction between the fillers and polymer matrix.

3.2. Rheological behaviors of EP suspensions

The rheological behaviors were characterized for neat EP and its suspensions containing $MoSe_2$ and LPP-$MoSe_2$ at 29 ℃. The linear relationship between shear stress (σ) and viscosity (η) and shear rate (γ) is illustrated in Fig. S3. There is no significant difference in the rheological behavior of EP and its suspensions containing $MoSe_2$ and LPP-$MoSe_2$. The σ increases with the increase of γ, while the η decreases with the increase of γ. The fit of σ and γ using power-law model proves that EP and its suspensions containing $MoSe_2$ and LPP-$MoSe_2$ are Newtonian fluid (Supplementary file S3).

3.3. Thermal property analysis

The thermal degradation behaviors of $MoSe_2$ and LPP-$MoSe_2$ were evaluated by thermogravimetric analysis (TGA) and the thermogravimetric (TG) curves are exhibited in Fig. 6 (a, b). Under air conditions (Fig. 6 (a)), the weight of $MoSe_2$ increases in the range of 200 – 300 ℃, which is assigned to the oxidation of $MoSe_2$ to MoO_3 and SeO_2 [34]. However, there is no weight gain process in LPP-$MoSe_2$, which is

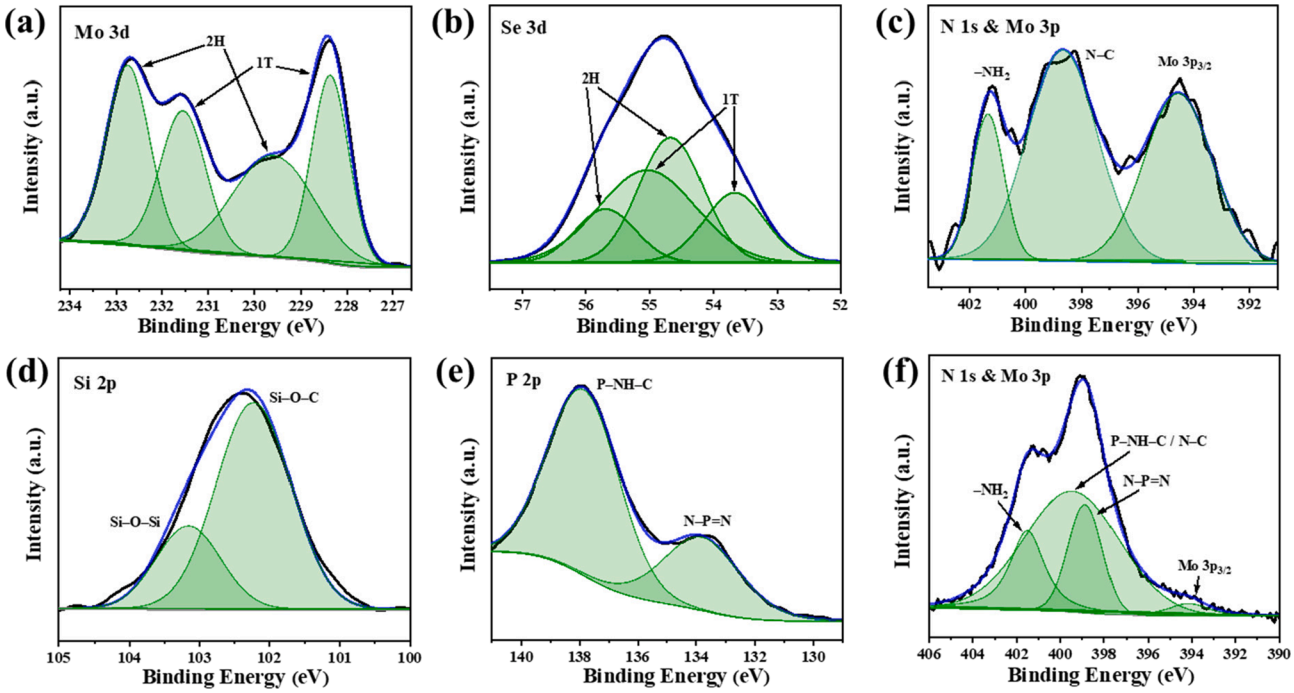

Fig. 4. High-resolution XPS spectra of $MoSe_2$ in the (a) Mo 3d, (b) Se 3d, and (c) N 1s & Mo 3p regions, high-resolution XPS spectra of LPP-$MoSe_2$ in the (d) Si 2p, (e) P 2p, and (f) N 1s & Mo 3p regions.

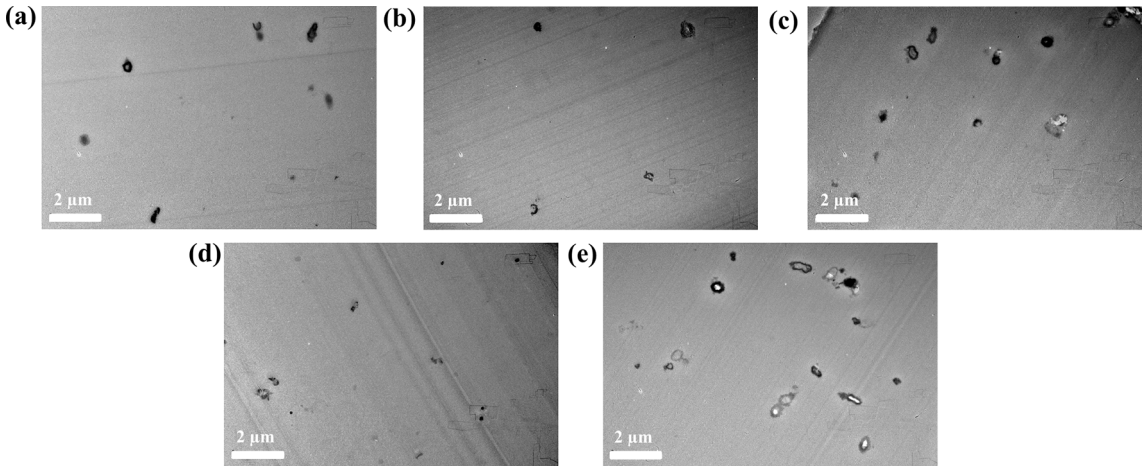

Fig. 5. TEM ultrathin section images of (a) EP/$MoSe_2$ 2.0; (b) EP/LPP-$MoSe_2$ 0.5; (c) EP/LPP-$MoSe_2$ 1.0; (d) EP/LPP-$MoSe_2$ 2.0 and (e) EP/LPP-$MoSe_2$ 3.0.

attributed to the encapsulation of APTES, LPP and their pyrolysis products on the surface of $MoSe_2$, preventing the preliminary oxidation of $MoSe_2$. As for LPP-$MoSe_2$, the occurrence of premature degradation is related to decomposition of the wrapped APTES and LPP. The further reduced weight can be attributed to the evaporation of the inserted ammonia species and octylamine molecules and the sublimation of SeO_2. Fig. 6(b) presents the TG curves of $MoSe_2$ and LPP-$MoSe_2$ under nitrogen. The 38.5% weight loss of $MoSe_2$ is mainly associated with evaporation of the inserted ammonia species and octylamine molecules. Besides, the LPP-$MoSe_2$ shows a relatively higher weight loss (52.2%), and the 13.7% additional weight loss corresponds to the degradation of the wrapped APTES and LPP.

To evaluate the effects of $MoSe_2$ and LPP-$MoSe_2$ on the thermal properties of polymer matrix, TG and derivative thermogravimetric (DTG) curves of EP thermosets were obtained through TGA analysis, as shown in Fig. 6(c-f). Several representative parameters including the onset degradation temperature ($T_{5\%}$) and the maximum degradation temperature (T_{max}) are listed in Table S2 to compare the thermal stability of these thermosets. In air, EP thermosets show a three-stage degradation process, corresponding to the evaporation of organic components, the degradation of EP chains and formed char (Fig. 6(c-d)). It is found from Table S2 that the addition of fillers reduces the $T_{5\%}$ of EP. This is attributed to the early degradation of the fillers, which accelerates the degradation of the EP matrix. It is worth noting that the char residues of EP composites at 800 ℃ are higher than neat EP (1.65 wt%), especially for EP/ LPP-$MoSe_2$ 2.0 (2.65 wt%). In nitrogen, the neat EP shows a one-stage mass loss, owing to the degradation of EP macromolecules. It can be observed from Fig. 6(e-f) that there are two-stage mass loss arising from the degradation of fillers and EP macromolecules. The addition of $MoSe_2$ and LPP-$MoSe_2$ greatly decreased the maximum thermal degradation rate and enhanced the char yield (800 ℃) of EP. These results manifest that the introduction of $MoSe_2$ and LPP-$MoSe_2$ improves the thermal stability of EP matrix.

3.4. Fire hazards

The flammability of EP and its composites under small-scale combustion conditions was evaluated by limiting oxygen index (LOI) and UL-94 tests. As recorded in Table 1, neat EP exhibits a low LOI value of 25%. In the UL-94 test, it burns vigorous once ignition and attains no rating. With the incorporation of $MoSe_2$, the LOI value of EP/$MoSe_2$ 2.0 raises to 29%, but fails the UL-94 test. The results indicate that $MoSe_2$ does not impart good flame retardancy to EP. When LPP-$MoSe_2$ is added, the LOI values of EP composite increase with the increasing addition amount of LPP-$MoSe_2$, where LPP-$MoSe_2$ 3.0 is elevated to 29%. Meanwhile, LPP-$MoSe_2$ shows prominent self-extinguishing ability after removing the ignition flame. EP/LPP-$MoSe_2$ 1.0 and EP/LPP-$MoSe_2$ 2.0 are rated as V-1, and EP/LPP-$MoSe_2$ 3.0 is further rated as V-0. In general, materials with higher LOI values than 26% will demonstrate self-extinguishing properties and are deemed as good flame retardant materials [53]. Consequently, the addition of LPP-$MoSe_2$ significantly improves the flame retardancy of EP.

As recognized as the best techniques to investigate the combustion characteristics of materials, the cone calorimeter based on the oxygen-consumption principle can simulate the real combustion environment to realize the measurement of various fire-related parameters. Heat release rate (HRR) and total heat release (THR) are recognized as the most crucial parameters to evaluate the flammability and flame retardancy of materials. As shown in Fig. 7(a-b) and Table 2, the neat EP exhibits a pointed HRR peak, resulting in the highest peak heat release rate (pHRR) (1251 KW/m^2) and THR (117.0 MJ/m^2) value, thus indicating a higher fire risk. The incorporation of $MoSe_2$ and LPP-$MoSe_2$ can promote the early combustion of EP composites and shorten the time to ignition (TTI). During combustion, both of them can decrease the pHRR and THR values of EP nanocomposites. Compared with neat EP, EP/LPP-$MoSe_2$ 3.0 exhibits the most effective reduction of pHRR (39.0%) and THR (25.0%). With the same additive amount, EP/LPP-$MoSe_2$ 2.0 and EP/$MoSe_2$ 2.0 demonstrate comparable flame retardant properties. The pHRR value of EP/$MoSe_2$ 2.0 (895 KW/m^2) is lower than EP/LPP-$MoSe_2$ 2.0 (1022 KW/m^2), whereas the THR value of EP/$MoSe_2$ 2.0 (105.9 MJ/m^2) is higher than EP/LPP-$MoSe_2$ 2.0 (96.0 MJ/m^2). Although these valuable parameters capture a image of the fire behavior of EP composites, their diversity obscures the assessment of the fire performance of composites and the efficiency of flame retardants. Hence, the flame retardancy index (FRI), as a universal criterion, was applied to evaluate the comprehensive flame retardancy by considering the main parameters (pHRR, THR, and TTI) in one [54]. The FRI was calculated from Eq. (1) [55].

$$FRI = \frac{\left[THR * \left(\frac{pHRR}{TTI}\right)\right]_{Neat\ Polymer}}{\left[THR * \left(\frac{pHRR}{TTI}\right)\right]_{Composite}} \quad (1)$$

It is highly desired to lower the THR and pHRR while prolong the TTI after introducing flame retardant. As a consequence, the higher FRI value indicates higher flame retardant efficiency. The flame retardancy of composites can be qualitatively defined as “Poor”, “Good” and “Excellent” when FRI < 1, 1 < FRI < 10 and 10 < FRI, respectively [56]. As shown in Table 2, the FRI values of all composites are >1, suggesting good flame retardancy performance. FRI is basically proportional with the loading of LPP-$MoSe_2$, while EP/LPP-$MoSe_2$ 3.0 brings about the highest FRI value (1.50).

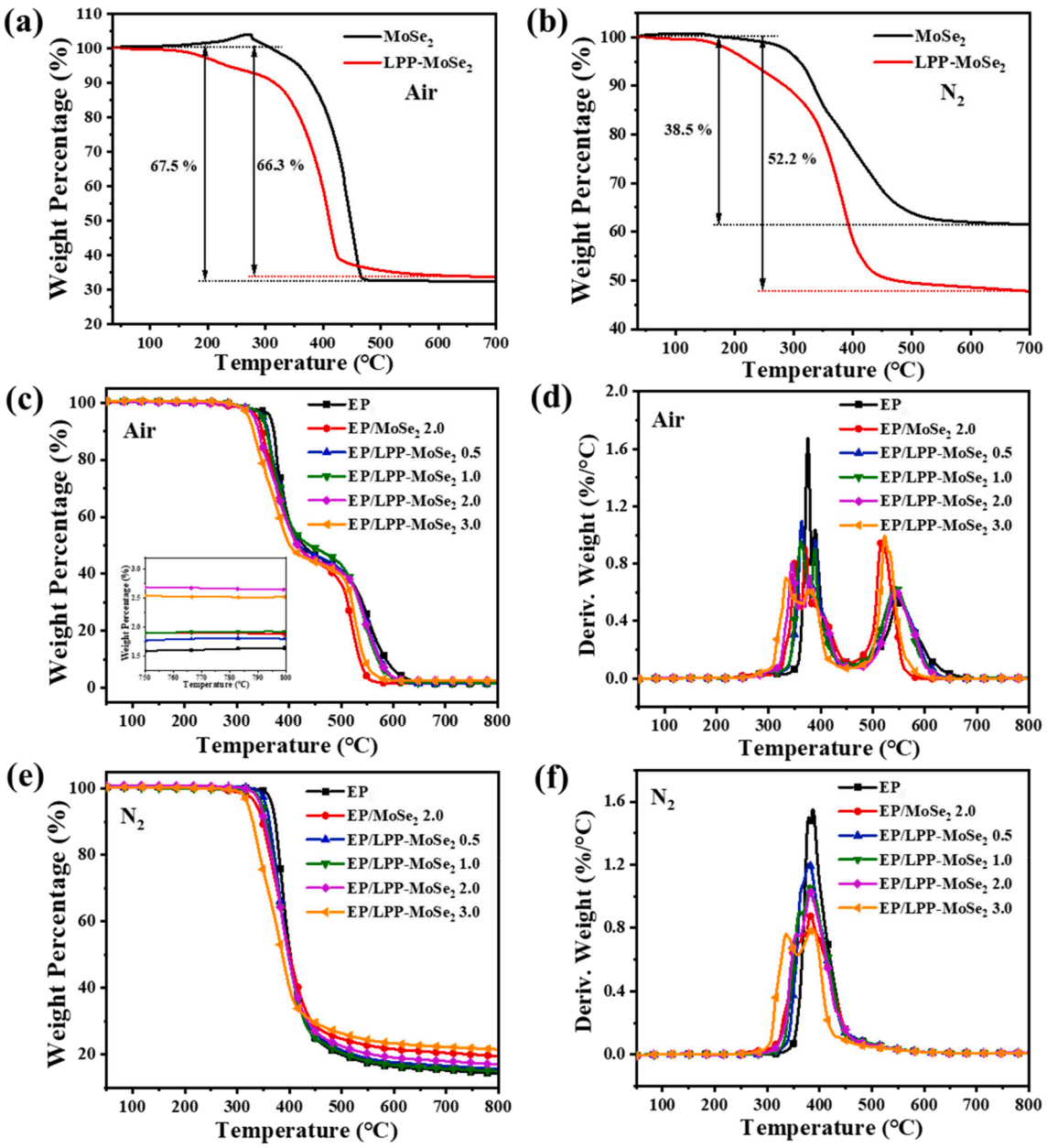

Fig. 6. (a-b) TG curves of $MoSe_2$ and LPP-$MoSe_2$; (c, e) TG and (d, f) DTG curves of EP and its composites.

Table 1
LOI and UL-94 results of EP and its composites.

Sample	UL-94 rating	t_1/t_2[a]	LOI (%)
EP	No rating	>30 / -[b]	25.0
EP/$MoSe_2$ 2.0	No rating	>30 / -[b]	29.0
EP/LPP-$MoSe_2$ 0.5	No rating	>30 / -[b]	27.0
EP/LPP-$MoSe_2$ 1.0	V-1	14 / 18	27.5
EP/LPP-$MoSe_2$ 2.0	V-1	18 / 7	28.0
EP/LPP-$MoSe_2$ 3.0	V-0	9 / 6	29.0

[a] t_1/t_2: average flame time after the first/second time ignition;
[b] : no second time ignition applied.

Based on cone calorimetry, the effective heat of combustion (EHC) reflects the combustion extent of volatiles in gas phase flame, which helps to investigate the flame retardant mechanism. The EHC of volatiles for EP/$MoSe_2$ 2.0 was increased, demonstrating the invalid gas-phase mechanism (Fig. 7(c)). Notably, the EHC values decreased with the increase of LPP-$MoSe_2$, which indicates the existence of gas-phase mechanism for LPP-$MoSe_2$ [57]. Besides, it is noteworthy that smoke and toxic gases are the most harmful and the main culprits causing casualties in actual fires. The exploration of effective additives that can realize high flame retardancy and low emission of toxic fumes for EP thermosets is an imperative task. Under the monitoring of the cone calorimeter, the total smoke production (TSP) curves of EP and its composites are illustrated in Fig. 7(d). Pure EP with a polyaromatic hydrocarbon structure is inclined to produce vast smoke during combustion, leading to high TSP values. It can be seen intuitively from Fig. 7 (d) that the introduction of LPP-$MoSe_2$ can significantly reduce the TSP value of EP. In comparison with pure EP, the TSP reduction of EP/LPP-$MoSe_2$ 2.0 reaches 31.3%, which outdistances EP/$MoSe_2$ 2.0 with the same additive dosage. This can be assigned to the combination effect of $MoSe_2$ and LPP. However, the TSP value of EP/LPP-$MoSe_2$ 3.0 is higher than EP/LPP-$MoSe_2$ 2.0. We reason that the organic radicals are converted into smoke particles under the enhanced vapor phase effect of LPP that brings about the decreased of fuels and declined of heat release.

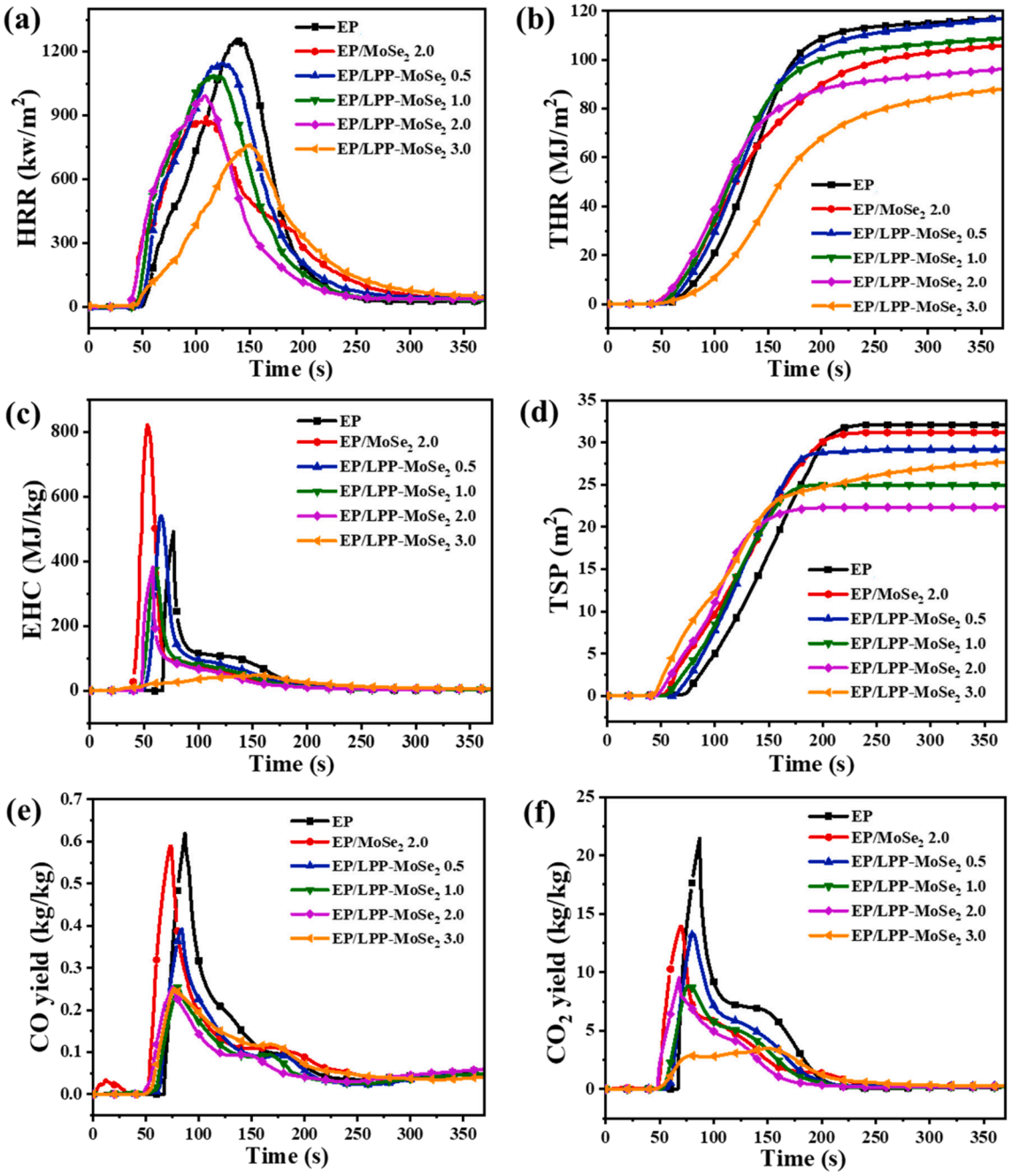

Fig. 7. (a) HRR, (b) THR, (c) EHC, (d) TSP, (e) CO yield and (f) CO_2 yield curves of EP and its composites.

Table 2
Cone calorimeter data of EP and its composites.

Sample	TTI (s)	pHRR (kW/m^2)	THR (MJ/m^2)	FRI	EHC (MJ/kg)	TSP (m^2)	CO yeild (kg/kg)	CO_2 yeild (kg/kg)
EP	64	1251.0	117.0	–	491.8	32.6	0.62	21.44
EP/$MoSe_2$ 2.0	56	895.0	105.9	1.35	780.0	31.2	0.59	13.95
EP/LPP-$MoSe_2$ 0.5	62	1146.5	116.8	1.06	541.1	29.1	0.40	13.23
EP/LPP-$MoSe_2$ 1.0	55	1087.7	108.6	1.07	373.7	25.0	0.25	8.83
EP/LPP-$MoSe_2$ 2.0	48	1022.0	96.0	1.12	383.7	22.4	0.25	9.53
EP/LPP-$MoSe_2$ 3.0	44	762.8	87.8	1.50	47.3	27.6	0.25	3.48

Furthermore, CO and CO_2 yields are also detected and depicted in Fig. 7 (e-f). The LPP-$MoSe_2$ shows impressive performance in lessening CO and CO_2 yields, which greatly weakens the fire risk of EP thermosets. Evidently, the inhibitory effect of LPP-$MoSe_2$ on CO and CO_2 is superior to $MoSe_2$, which further proves the mutual promotion effect between LPP and $MoSe_2$ in improving the fire safety of EP.

3.5. Flame retardant mechanism

3.5.1. Gas phase analysis

To evaluate the thermal degradation mechanism of EP thermosets, which is essential for the study of flame retardancy, the gaseous pyrolysis products were collected by using thermogravimetric analysis-fourier transform infrared spectroscopy (TG-IR). Fig. 8(a) presents the FTIR spectra of EP and EP/LPP-$MoSe_2$ 3.0 at the maximum thermal decomposition rate. The main detected pyrolysis products for EP and EP/LPP-$MoSe_2$ 3.0 are H_2O and/or phenol (3650 cm^{-1}), hydrocarbons (2930 cm^{-1}), CO_2 (2358 cm^{-1}), CO (2190 cm^{-1}), carbonyl-containing compounds (1740 cm^{-1}) and aromatics (1510 cm^{-1}) [58]. Remarkably, the total gaseous products of EP/LPP-$MoSe_2$ 3.0 is lower than EP (Fig. 8 (b)). Associated with TGA results (Fig. 6(e)), the introduction of LPP-$MoSe_2$ 3.0 facilitates the char formation, which can effectively impede the escape of gaseous pyrolysis products. To gain more insight to the influence of LPP-$MoSe_2$ on the thermal degradation behavior of EP, the absorbance intensities of individual pyrolysis products are illustrated in Fig. 9. The maximum absorbance intensities of these pyrolysis products are significantly decreased with the incorporation of 3 wt% LPP-$MoSe_2$. The reduction in aromatics and hydrocarbons implies lower concentration of flammable gases, which helps reduce heat release and smoke generation. The addition of LPP-$MoSe_2$ can also efficiently suppress the volatilization of CO, which present a major smoke toxicity hazard. It well coincides with the cone calorimeter results that LPP-$MoSe_2$ performs well in reducing the fire risk of EP. Moreover, under external heating, EP undergoes free radical chain degradation reactions with oxygen in the air, which produces combustible volatiles [20]. The decomposition of LPP will generate incombustible gases (NH_3 or N_2), which dilutes the flammable volatiles and oxygen and takes heat away. Meanwhile, the produced PO· and PO_2· during the LPP combustion can efficiently quench the main reactants (H· and HO·) in the combustion zone, thus terminating the chain reaction of combustion [45].

3.5.2. Condensed phase analysis

To elucidate the mechanism for the flame retardance of LPP-$MoSe_2$, the char residues of EP thermosets obtained from cone test were surveyed. Fig. 10 shows the digital photos of char residues, and obvious difference appears among EP and its composites. There are few incomplete char residues remains for pure EP, implying the sufficient combustion of EP. The addition of $MoSe_2$ has little effect on char formation, leaving fewer char residues in EP/$MoSe_2$ 2.0. By contrast, more complete and dense char residues are formed by adding only 0.5 wt% LPP-$MoSe_2$. The height and integrity of char residues increased continuously with the increase of the addition amount of LPP-$MoSe_2$. The gases (NH_3 or N_2) generated from the decomposition of LPP will promote the intumescence of the char layer [20]. The char expansion effect from LPP and the combined catalytic carbonization effect of LPP and $MoSe_2$ account for the formation of more compact and continuous expanded char layer.

The microstructures of char residues were also characterized by SEM. There are openings and cracks on the surface of char residues of neat EP (Fig. 11). After incorporation of $MoSe_2$, EP/$MoSe_2$ 2.0 exhibits fluffy porous char layer structure, which is attributed to the limited catalytic carbonization effect of $MoSe_2$. In addition, the synergic effect between LPP and $MoSe_2$ triggered the increase and expansion of carbon layers. The EP composites containing LPP-$MoSe_2$ feature a fluffy char layer structure with closed holes on its surface. The fluffy char residues are incombustible, which can weaken the heat transfer within polymer and prevent gas diffusion. The element distribution maps of char residues for EP thermosets are also supplied in Fig. S4. The char residues of neat EP are mainly composed of C and O, while Mo and Se are detected after the introduction of $MoSe_2$. As for EP/LPP-$MoSe_2$ 3.0, the P and Si elements were further detected. The distinct P and Si elements for EP/LPP-$MoSe_2$ 3.0 stem from the pyrolysis of LPP and APTES. The produced small molecules such as phosphoric acid and metaphosphoric acid can form a non-volatile film on the matrix surface to prevent the infiltration of oxygen and combustible gases, thus inhibiting the combustion reaction.

The heat resistance and thermostability of char residues are also important for flame retardation, which is related to their graphitization degree. The structural constituents of char residues were elucidated by Raman spectroscopy studies. Similar characteristic peaks were demonstrated for all EP thermosets at 1365 and 1596 cm^{-1} assigned to D and G bands, respectively (Fig. 11) [59]. The area ratio of D to G peak (I_D/I_G) is the key index for graphitization degree, and lower value (I_D/I_G) indicates higher graphitization degree. The I_D/I_G value of neat EP was calculated to be 3.21, higher than those of EP composites. The introduction of $MoSe_2$ and LPP-$MoSe_2$ give rise to the decline of I_D/I_G value, demonstrating the elevated graphitization degree. Thereinto, EP/LPP-$MoSe_2$ 3.0 exhibits the lowest I_D/I_G value, indicating the highest graphitization degree. The high quality char layers of EP/LPP-$MoSe_2$ 3.0 facilitate to shield the underlying resin.

XPS analysis was also performed to investigate the detailed composition of char residues. In the XPS survey spectra of char residues (Fig. 12 (a)), pure EP exhibits three signals corresponding to C, N and O. Additional P, Si, Mo and Se signals are detected in EP/LPP-$MoSe_2$ 3.0, indicating the presence of substances containing P, Si, Mo and Se in the char residue. Simultaneously, the high-resolution C 1 s, Si 2p and P 2p spectra of EP/LPP-$MoSe_2$ 3.0 are depicted in Fig. 12(b-d). For C 1 s species, three peaks located in 284.8, 285.9 and 289.6 eV are asigned to C=O, C–O and C–C, respectively [60]. The Si 2p signal in Fig. 12(c) can be deconvolved into two peaks at 101.7 and 103.4 eV, demonstrating the formation of Si–C bond and silicon oxide compounds [61]. It is beneficial for the formation of high-quality char residues. Three peaks at 133.8, 137.1 and

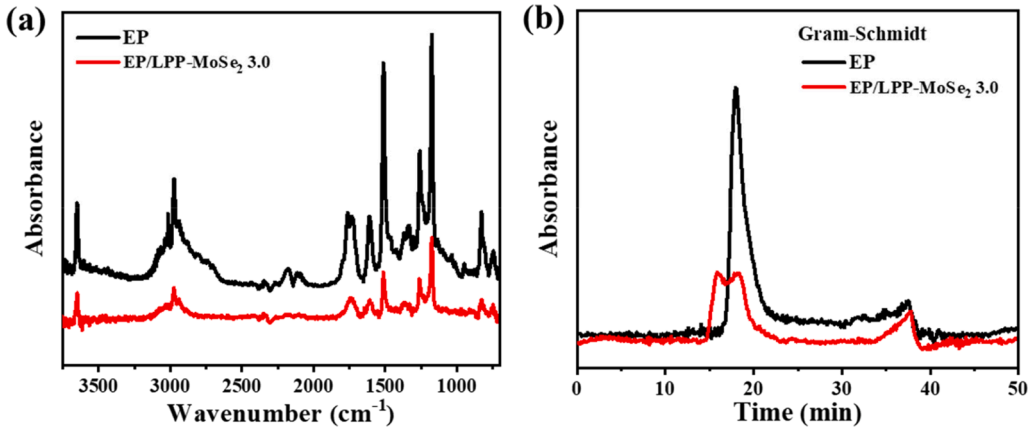

Fig. 8. TG-IR results of EP and EP/LPP-$MoSe_2$ 3.0; (a) FTIR spectra at the maximum decomposition rate; (b) Gram-Schmidt curves.

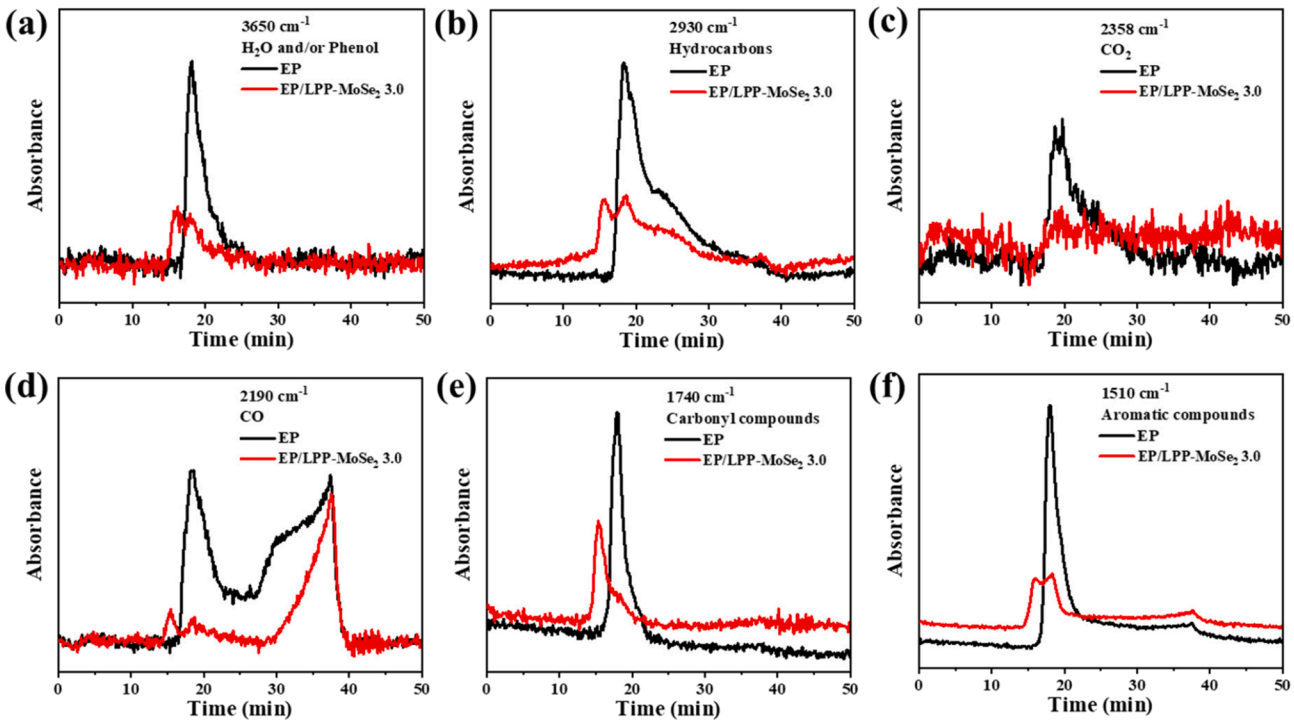

Fig. 9. Absorbance of volatilized pyrolysis products for EP and EP/LPP-$MoSe_2$ 3.0.

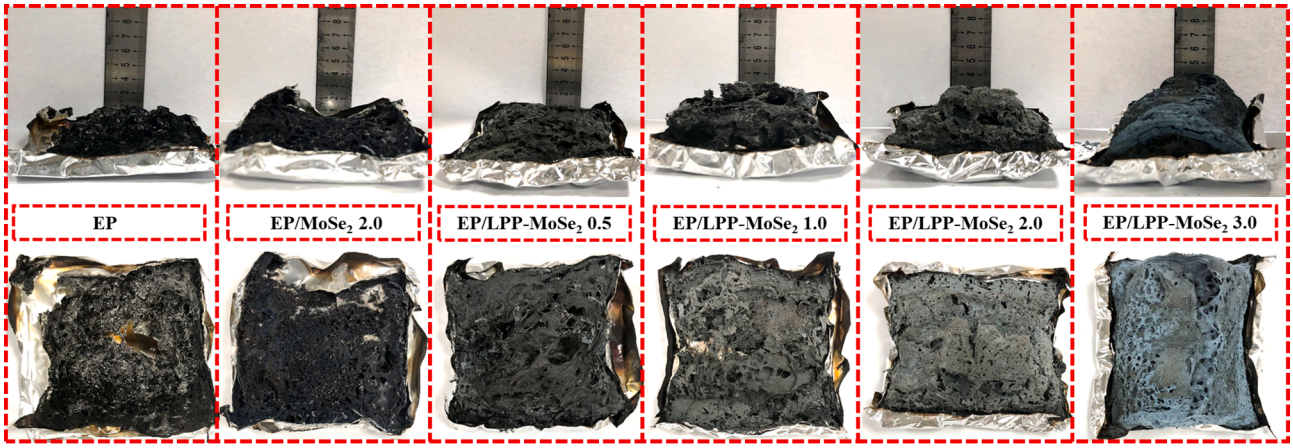

Fig. 10. Digital pictures of the external residues from side view and top view of pure EP and its composites.

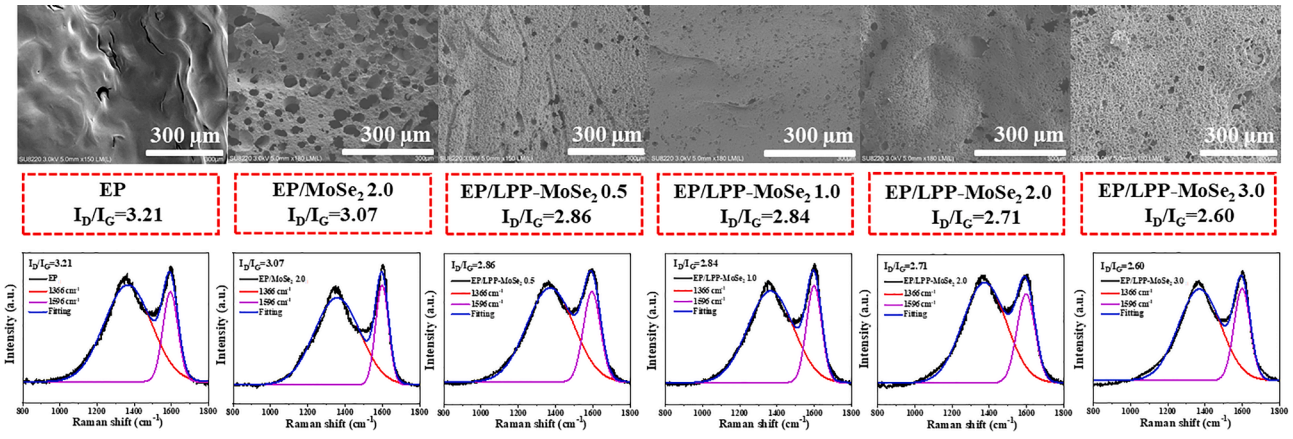

Fig. 11. SEM images and Raman spectra of exterior char residues.

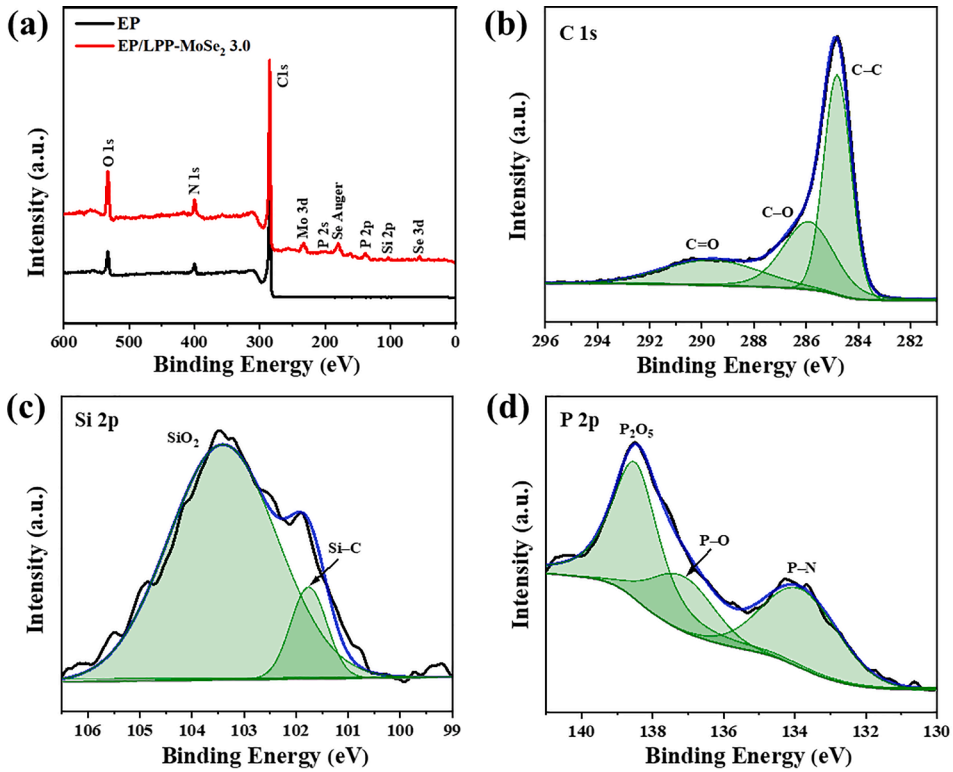

Fig. 12. (a) XPS spectra of char residues for EP and EP/LPP-$MoSe_2$ 3.0; high-resolution XPS spectra of char residue for EP/LPP-$MoSe_2$ 3.0 in the (b) C 1 s, (c) Si 2p and (d) P 2p regions.

138.4 eV are observed in the P 2p spectrum, corresponding to P–N, P–O and P_2O_5, which reveals the generation of cross-linked phosphoric-nitric oxides [45]. The formed PO_x can be derived from phosphoric acid or metaphosphoric acid, which function in condensed phase to facilitate the formation of highly stable protective char layers.

On the basis of above analysis, a feasible flame retardant mechanism is propounded. Two-phase mechanism is employed to explain the contribution of LPP-$MoSe_2$ to the fire retardation of EP. In the gas phase, the decomposition of LPP will generate incombustible gases (NH_3 or N_2), which contributes to the formation of intumescent char layer and the dilution of flammable gases and oxygen. Meanwhile, the produced PO· and PO_2· during the LPP combustion can efficiently quench the active radicals in the combustion zone, such as H· and HO·, thus terminating the chain reaction of combustion. In the condensed phase, LPP-$MoSe_2$ is excellent from the viewpoint of combined catalytic carbonization effect. The small molecular substances, such as phosphoric acid or metaphosphoric acid, generated from the thermal decomposition of LPP can not only promote the dehydration and carbonization of EP matrix, but also form a non-volatile protective film on the EP surface to isolate air. Moreover, $MoSe_2$ as transition metal compound is capable of catalytic carbonization, which facilitates the formation of high-quality char layers. The combination of the advantages of LPP and $MoSe_2$ affords superior protective char layers, which blocks the infiltration of oxygen and flammable gases and the escape of toxic smoke and gases. It can also restrain mass and heat transfer and impede the pyrolysis of underlying polymer, thereby improving the fire safety of EP.

3.6. *Mechanical properties*

To evaluate the mechanical properties of EP composites, beam impact test and tensile test were carried out. It is observed from Fig. 13 (a) that the un-notched impact strength of EP composites are enhanced

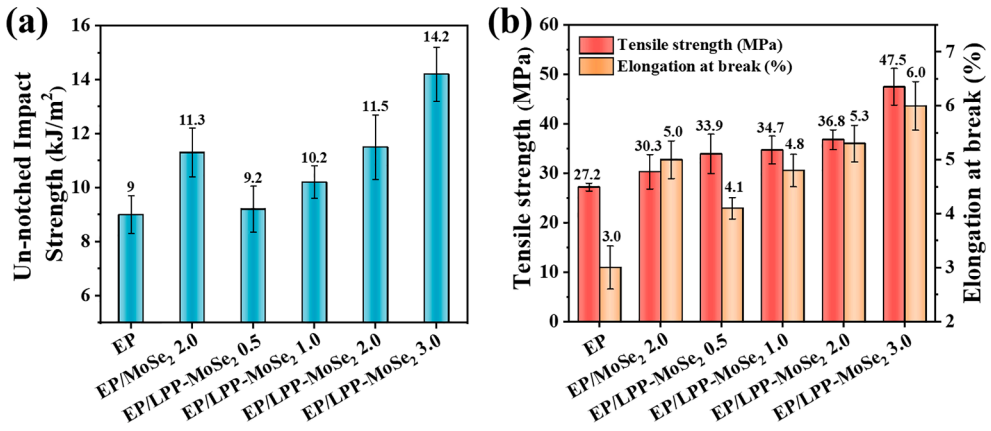

Fig. 13. (a) Impact strength and (b) tensile strength and elongation at break of EP and its composites.

after the incorporation of $MoSe_2$ and LPP-$MoSe_2$. The impact strength of neat EP is only 9 kJ/m^2, while EP/$MoSe_2$ 2.0 can reach up to 11.3 kJ/m^2. EP/LPP-$MoSe_2$ 3.0 exhibits the most significant elevation (57.8%) compared to pure EP, implying an evident toughening effect of LPP-$MoSe_2$. As illustrated in Fig. 13 (b), the tensile strength and elongation at break of neat EP are 27.2 MPa and 3.0%, respectively, with intrinsic brittleness. The addition of $MoSe_2$ and LPP-$MoSe_2$ increases the tensile strength of EP composites, suggesting their reinforcing effect. The tensile strength of EP/$MoSe_2$ 2.0 presents an improvement of 11.4% in comparison with neat EP. The tensile strength also increases with the addition of 0.5 wt%, 1 wt%, 2 wt%, and 3 wt% of LPP-$MoSe_2$, which indicates the nano-enhancement effect of $MoSe_2$ and LPP-$MoSe_2$. Similar trend of elongation at break is also observed for EP composites. EP/LPP-$MoSe_2$ 3.0 displays the most prominent improvement in elongation at break, which is 100% higher than neat EP. The increment of elongation at break indicates the improved fracture toughness of EP composites. It is acknowledged that good dispersion state of additives is the prerequisite to achieve the expected mechanical performances. Good dispersion state of LPP-$MoSe_2$ in EP has been verified in the TEM ultrathin section images (Fig. 5). Moreover, LPP-$MoSe_2$ nanotubes with amino groups on its surface can act as physical cross-linking points in the EP matrix to improve the strength of the composites. Simultaneously, the LPP-$MoSe_2$ with nanotube structure is apt to form pinning effect with polymer interface, thus forming a stable network structure [62]. It is conducive to the transfer and homogenization of stress, leading to the strengthening and toughening of the EP matrix. Hence, achieving flame retardation and mechanical improvement objective through designing EP/LPP-$MoSe_2$ nanocomposites is thus confirmed by this work.

4. Conclusions

Altogether, for the purpose of improving the fire safety and toughness of EP, we designed a novel LPP-$MoSe_2$ hybrid with nanotube structure to cope with these obstacles in the practical application of EP. Our data demonstrate that LPP-$MoSe_2$ shows impressive performance in flame retardation, smoke suppression and toughening. The microstructural analysis of EP/LPP-$MoSe_2$ 2.0 verifies the good dispersion state of LPP-$MoSe_2$ in EP. TGA results indicate that the addition LPP-$MoSe_2$ greatly decreases the maximum thermal degradation rate and enhances the char residues (800 ℃) of EP. In comparison with neat EP with a LOI value of 25% and no rating in UL-94 test, EP/LPP-$MoSe_2$ 3.0 obtains a high LOI value of 29% and reaches V-0 rating in UL-94 test. Based on the cone calorimetry, EP/LPP-$MoSe_2$ 3.0 exhibits the most effective reduction in pHRR (39.0%) and THR (24.8%). Comprehensively evaluated by FRI, EP/LPP-$MoSe_2$ 3.0 shows good flame retardancy performance and brings about the highest FRI value (1.50). The significantly decreased EHC for EP/LPP-$MoSe_2$ 3.0 reveals the presence of gas-phase mechanism for LPP-$MoSe_2$. More importantly, the introduction of LPP-$MoSe_2$ can efficiently depress the TSP value (31.3% for EP/LPP-$MoSe_2$ 2.0) and the yields of CO and CO_2, well below neat EP. The TG-FTIR results are well coincide with the cone calorimeter results that LPP-$MoSe_2$ performs well in suppressing the volatilization of flammable gases and toxic gases, thereby revealing the appealing properties of LPP-$MoSe_2$ for constructing EP thermosets with prominent flame retardancy. It is pointed out that two-phase mechanism is employed to explain the contribution of LPP-$MoSe_2$ to the fire retardation of EP. The gas dilution and free radical quenching effect in the gas phase can retard the combustion of EP, while the catalytic carbonization effect in the condensed phase promotes the formation of superior protective char layers. Meanwhile, compared to pure EP, EP/LPP-$MoSe_2$ 3.0 exhibits significant elevation in impact strength of (57.8%), tensile strength (74.6%) and elongation at break (100%) of EP, implying a strengthening and toughening effect of LPP-$MoSe_2$. These merits offer LPP-$MoSe_2$ great potential for designing high-performance EP composites.

Declaration of Competing Interest

The authors declare that they have no known competing financial interests or personal relationships that could have appeared to influence the work reported in this paper.

Acknowledgements

The financial support from the National Natural Science Foundation of China (51973203) and the China Postdoctoral Special Funding (2019TQ0309, 2020M671904) are gratefully acknowledged.

Appendix A. Supplementary data

Supplementary data to this article can be found online at https://doi.org/10.1016/j.cej.2021.131839.

References

[1] W. Li, D. Liu, N.a. Yang, J. Wang, M. Huang, L. Liu, X. Peng, G. Wang, X.-F. Yu, P. K. Chu, Molybdenum diselenide – black phosphorus heterostructures for electrocatalytic hydrogen evolution, Appl. Surf. Sci. 467-468 (2019) 328–334.
[2] D. Geng, H.Y. Yang, Recent advances in growth of novel 2D materials: beyond graphene and transition metal dichalcogenides, Adv. Mater. 30 (2018) 1800865.
[3] X. Zhang, X.-F. Qiao, W. Shi, J.-B. Wu, D.-S. Jiang, P.-H. Tan, Phonon and Raman scattering of two-dimensional transition metal dichalcogenides from monolayer, multilayer to bulk material, Chem. Soc. Rev. 44 (9) (2015) 2757–2785.
[4] J. Zhang, W. Kang, M. Jiang, Y.u. You, Y. Cao, T.-W. Ng, D.Y.W. Yu, C.-S. Lee, J. Xu, Conversion of 1T-$MoSe_2$ to 2H-$MoS_{2x}Se_{2-2x}$ mesoporous nanospheres for superior sodium storage performance, Nanoscale. 9 (4) (2017) 1484–1490.
[5] G.H. Han, D.L. Duong, D.H. Keum, S.J. Yun, Y.H. Lee, van der Waals metallic transition metal dichalcogenides, Chem. Rev. 118 (13) (2018) 6297–6336.
[6] Z. Lei, Y. Zhou, P. Wu, Simultaneous exfoliation and functionalization of $mose_2$ nanosheets to prepare "smart" nanocomposite hydrogels with tunable dual stimuli-responsive behavior, Small. 12 (23) (2016) 3112–3118.
[7] X. He, L. Zhang, R. Chua, P.K.J. Wong, A. Arramel, Y.P. Feng, S.J. Wang, D. Chi, M. Yang, Y.L. Huang, A.T.S. Wee, Selective self-assembly of 2,3-diaminophenazine molecules on $MoSe_2$ mirror twin boundaries, Nat. Commun. 10 (2019) 2847.
[8] S. Wang, X. Cui, C. Jian, H. Cheng, M. Niu, J. Yu, J. Yan, W. Huang, Stacking-engineered heterostructures in transition metal dichalcogenides, Adv. Mater. 33 (16) (2021) 2005735, https://doi.org/10.1002/adma.v33.1610.1002/adma.202005735.
[9] H. Xie, S. Jiang, D.A. Rhodes, J.C. Hone, J. Shan, K.F. Mak, Tunable exciton-optomechanical coupling in suspended monolayer $MoSe_2$, Nano. Lett. 21 (6) (2021) 2538–2543.
[10] J. Gao, B. Li, J. Tan, P. Chow, T.-M. Lu, N. Koratkar, Aging of transition metal dichalcogenide monolayers, ACS. Nano. 10 (2) (2016) 2628–2635.
[11] L.J. Pi, L. Li, K.L. Liu, Q.F. Zhang, H.Q. Li, T.Y. Zhai, Recent progress on 2D noble-transition-metal dichalcogenides, Adv. Funct. Mater. 29 (2019) 1904932.
[12] X. Chia, A.Y.S. Eng, A. Ambrosi, S.M. Tan, M. Pumera, Electrochemistry of nanostructured layered transition-metal dichalcogenides, Chem. Rev. 115 (21) (2015) 11941–11966.
[13] Y. Ma, S. Kolekar, H. Coy Diaz, J. Aprojanz, I. Miccoli, C. Tegenkamp, M. Batzill, Metallic twin grain boundaries embedded in $mose_2$ monolayers grown by molecular beam epitaxy, ACS Nano. 11 (5) (2017) 5130–5139.
[14] H. Qu, S.H. He, Y. Su, Y.L. Zhang, H.Q. Su, $MoSe_2$: a promising non-noble metal catalyst for direct ethanol synthesis from syngas, Fuel. 281 (2020), 118760.
[15] J. Wang, C. Ma, X. Mu, W. Cai, L. Liu, X. Zhou, W. Hu, Y. Hu, Construction of multifunctional $MoSe_2$ hybrid towards the simultaneous improvements in fire safety and mechanical property of polymer, J. Hazard. Mater. 352 (2018) 36–46.
[16] S. Qiu, Y. Shi, B. Wang, X. Zhou, J. Wang, C. Wang, C.S.R. Gangireddy, R.K. K. Yuen, Y. Hu, Constructing 3D polyphosphazene Nanotube@Mesoporous Silica@Bimetallic phosphide ternary nanostructures via layer-by-layer method: synthesis and applications, ACS Appl. Mater. Inter. 9 (27) (2017) 23027–23038.
[17] X. Zhou, S. Qiu, J. Liu, M. Zhou, W. Cai, J. Wang, F. Chu, W. Xing, L. Song, Y. Hu, Construction of porous g-C_3N_4@PPZ tubes for high performance BMI resin with enhanced fire safety and toughness, Chem. Eng. J. 401 (2020), 126094.
[18] M. Deng, S.G. Kumbar, L.S. Nair, A.L. Weikel, H.R. Allcock, C.T. Laurencin, Biomimetic structures: biological implications of dipeptide-substituted polyphosphazene-polyester blend nanofiber matrices for load-bearing bone regeneration, Adv. Funct. Mater. 21 (2011) 2641–2651.
[19] S. Rothemund, I. Teasdale, Preparation of polyphosphazenes: a tutorial review, Chem. Soc. Rev. 45 (19) (2016) 5200–5215.
[20] X. Zhou, S. Qiu, X. Mu, M. Zhou, W. Cai, L. Song, W. Xing, Y. Hu, Polyphosphazenes-based flame retardants: a review, Compos. Part B-Eng. 202 (2020) 108397, https://doi.org/10.1016/j.compositesb:2020.108397.
[21] Y.i. Ren, Z. Li, H.R. Allcock, Molecular Engineering of polyphosphazenes and SWNT hybrids with potential applications as electronic materials, Macromolecules. 51 (14) (2018) 5011–5018.

[22] V. Poscher, I. Teasdale, Y. Salinas, Surfactant-free synthesis of cyclomatrix and linear organosilica phosphazene-based hybrid nanoparticles, ACS Appl. Nano. Mater. 2 (2) (2019) 655–660.
[23] C. Tong, Z. Tian, C. Chen, Z. Li, T. Modzelewski, H.R. Allcock, Synthesis and characterization of trifluoroethoxy polyphosphazenes containing polyhedral oligomeric silsesquioxane (POSS) side groups, Macromolecules. 49 (4) (2016) 1313–1320.
[24] T. Mayer-Gall, D. Knittel, J.S. Gutmann, K. Opwis, Permanent flame retardant finishing of textiles by allyl-functionalized polyphosphazenes, ACS Appl. Mater. Inter. 7 (18) (2015) 9349–9363.
[25] P. Chen, Z. Wu, T. Guo, Y. Zhou, M. Liu, X. Xia, J. Sun, L. Lu, X. Ouyang, X. Wang, Y. Fu, J. Zhu, Strong chemical interaction between lithium polysulfides and flame-retardant polyphosphazene for lithium-sulfur batteries with enhanced safety and electrochemical performance, Adv. Mater. 33 (2021) 2007549.
[26] X. Zhou, S. Qiu, W. Xing, C.S.R. Gangireddy, Z. Gui, Y. Hu, Hierarchical polyphosphazene@Molybdenum disulfide hybrid structure for enhancing the flame retardancy and mechanical property of epoxy resins, ACS Appl. Mater. Inter. 9 (34) (2017) 29147–29156.
[27] D.A. Nagarjuna Amarnath, B. Lochab, Eco-friendly halogen-free flame retardant cardanol polyphosphazene polybenzoxazine networks, ACS Sustain. Chem. Eng. 6 (2018) 389–402.
[28] X. Mu, D. Wang, Y. Pan, W. Cai, L. Song, Y. Hu, A facile approach to prepare phosphorus and nitrogen containing macromolecular covalent organic nanosheets for enhancing flame retardancy and mechanical property of epoxy resin, Compos. Part B-Eng. 164 (2019) 390–399.
[29] B. Yuan, Y. Wang, G. Chen, F. Yang, H. Zhang, C. Cao, B. Zuo, Nacre-like graphene oxide paper bonded with boric acid for fire early-warning sensor, J. Hazard. Mater. 403 (2021), 123645.
[30] Y. Xiao, Z. Jin, L. He, S. Ma, C. Wang, X. Mu, L. Song, Synthesis of a novel graphene conjugated covalent organic framework nanohybrid for enhancing the flame retardancy and mechanical properties of epoxy resins through synergistic effect, Compos. Part B-Eng. 182 (2020), 107616.
[31] X. Mu, W. Cai, Y. Xiao, L. He, X. Zhou, H.-J. Wang, W. Guo, W. Xing, L. Song, A novel strategy to prepare COFs based BN co-doped carbon nanosheet for enhancing mechanical performance and fire safety to PVA nanocomposite, Compos. Part B-Eng. 198 (2020), 108218.
[32] C. Ma, S. Qiu, B. Yu, J. Wang, C. Wang, W. Zeng, Y. Hu, Economical and environment-friendly synthesis of a novel hyperbranched poly (aminomethylphosphine oxide-amine) as co-curing agent for simultaneous improvement of fire safety, glass transition temperature and toughness of epoxy resins, Chem. Eng. J. 322 (2017) 618–631.
[33] W. Yu, J. Fu, X. Dong, L. Chen, H. Jia, L. Shi, Highly populated and nearly monodispersed nanosilica particles in an organic medium and their epoxy nanocomposites, ACS Appl. Mater. Inter. 5 (18) (2013) 8897–8906.
[34] J. Zhang, M. Wu, T. Liu, W. Kang, J. Xu, Hierarchical nanotubes constructed from interlayer-expanded $MoSe_2$ nanosheets as a highly durable electrode for sodium storage, J. Mater. Chem. A. 5 (47) (2017) 24859–24866.
[35] G.A. Carriedo, F.J. García Alonso, P. Gómez-Elipe, J.I. Fidalgo, J.L. GarcíaÁlvarez, A. Presa-Soto, A simplified and convenient laboratory-scale preparation of ^{14}N or ^{15}N high molecular weight poly(dichlorophosphazene) directly from PCl_5, Chemistry. 9 (16) (2003) 3833–3836.
[36] X. Wang, S. Wang, W. Wang, H. Li, X. Liu, X. Gu, S. Bourbigot, Z. Wang, J. Sun, S. Zhang, The flammability and mechanical properties of poly (lactic acid) composites containing Ni-MOF nanosheets with polyhydroxy groups, Compos. Part B-Eng. 183 (2020) 107568, https://doi.org/10.1016/j.compositesb:2019.107568.
[37] Y. Xiao, C. Ma, Z. Jin, J. Wang, L. He, X. Mu, L. Song, Y. Hu, Functional covalent organic framework for exceptional Fe^{2+}, Co^{2+} and Ni^{2+} removal: an upcycling strategy to achieve water decontamination and reutilization as smoke suppressant and flame retardant simultaneously, Chem. Eng. J. 421 (2021) 127837, https://doi.org/10.1016/j.cej.2020.127837.
[38] Y. Xiao, C. Ma, Z. Jin, C. Wang, J. Wang, H. Wang, X. Mu, L. Song, Y. Hu, Functional covalent organic framework illuminate rapid and efficient capture of Cu (II) and reutilization to reduce fire hazards of epoxy resin, Sep. Purif. Technol. 259 (2021), 118119.
[39] K. Hayashi, M. Nakamura, H. Miki, S. Ozaki, M. Abe, T. Matsumoto, K. Ishimura, Near-infrared fluorescent silica/porphyrin hybrid nanorings for in vivo cancer imaging, Adv. Funct. Mater. 22 (17) (2012) 3539–3546.
[40] M. Sundhoro, J. Park, B. Wu, M. Yan, Synthesis of polyphosphazenes by a fast perfluoroaryl azide-mediated staudinger reaction, Macromolecules. 51 (12) (2018) 4532–4540.
[41] X. Mu, X. Zhou, W. Wang, Y. Xiao, C. Liao, H. Longfei, Y. Kan, L. Song, Design of compressible flame retardant grafted porous organic polymer based separator with high fire safety and good electrochemical properties, Chem. Eng. J. 405 (2021), 126946.
[42] Z. Chen, L. Guo, H. Yan, H. Yao, L. Li, Q.i. Liu, Amino functionalization of graphene/graphene-like $MoSe_2$ hybrids as lubricant additives for bismaleimide composites: preparation, mechanical and tribological properties, Compos. Part B-Eng. 161 (2019) 263–271.
[43] M. Ojha, M. Deepa, Molybdenum selenide nanotubes decorated carbon net for a high performance supercapacitor, Chem. Eng. J. 368 (2019) 772–783.
[44] B. Yuan, Y. Sun, X. Chen, Y. Shi, H. Dai, S. He, Poorly-/well-dispersed graphene: abnormal influence on flammability and fire behavior of intumescent flame retardant, Compos. Part. A-Appl. S. 109 (2018) 345–354.
[45] Y. Zhou, F. Chu, S. Qiu, W. Guo, S. Zhang, Z. Xu, W. Hu, Y. Hu, Construction of graphite oxide modified black phosphorus through covalent linkage: an efficient strategy for smoke toxicity and fire hazard suppression of epoxy resin, J. Hazard. Mater. 399 (2020), 123015.
[46] W.Z. Tian, B. Xi, Z. Feng, H.B. Li, J.K. Feng, S.L. Xiong, Sulfiphilic few-layered $MoSe_2$ nanoflakes decorated rGO as a highly efficient sulfur host for lithium-sulfur batteries, Adv. Energy. Mater. 9 (2019) 1901896.
[47] N. Li, L. Sun, K. Wang, J. Zhang, X. Liu, Anchoring $MoSe_2$ nanosheets on N-doped carbon nanotubes as high performance anodes for potassium-ion batteries, Electrochimica. Acta. 360 (2020), 123983.
[48] B. Qu, C. Li, C. Zhu, S. Wang, X. Zhang, Y. Chen, Growth of $MoSe_2$ nanosheets with small size and expanded spaces of (002) plane on the surfaces of porous N-doped carbon nanotubes for hydrogen production, Nanoscale. 8 (38) (2016) 16886–16893.
[49] J.K. Kim, K.E. Lim, W.J. Hwang, Y.C. Kang, S.-K. Park, Hierarchical tubular-structured $MoSe_2$ nanosheets/N-doped carbon nanocomposite with enhanced sodium storage properties, ChemSusChem. 13 (6) (2020) 1546–1555.
[50] J. Wang, D. Zhang, Y. Zhang, W. Cai, C. Yao, Y. Hu, W. Hu, Construction of multifunctional boron nitride nanosheet towards reducing toxic volatiles (CO and HCN) generation and fire hazard of thermoplastic polyurethane, J. Hazard. Mater. 362 (2019) 482–494.
[51] X. Mu, Y. Pan, C. Ma, J. Zhan, L. Song, Novel Co_3O_4/covalent organic frameworks nanohybrids for conferring enhanced flame retardancy, smoke and CO suppression and thermal stability to polypropylene, Mater. Chem. Phys. 215 (2018) 20–30.
[52] X. Chen, Y. Ma, Y.-J. Cheng, A. Zhang, W. Liu, H. Zhou, Synergistic effect between a novel silane-containing hyperbranched polyphosphamide and ammonium polyphosphate on the flame retardancy and smoke suppression of polypropylene composites, Polym. Degrad. Stabil. 181 (2020), 109348.
[53] L.L. Pan, G.Y. Li, Y.C. Su, J.S. Lian, Fire retardant mechanism analysis between ammonium polyphosphate and triphenyl phosphate in unsaturated polyester resin, Polym. Degrad. Stabil. 97 (9) (2012) 1801–1806.
[54] E. Movahedifar, H. Vahabi, M.R. Saeb, S. Thomas, Flame retardant epoxy composites on the road of innovation: an analysis with flame retardancy index for future development, Molecules. 24 (2019).
[55] H. Vahabi, F. Laoutid, M. Mehrpouya, M.R. Saeb, P. Dubois, Flame retardant polymer materials: an update and the future for 3D printing developments, Mat. Sci. Eng. R. 144 (2021) 100604, https://doi.org/10.1016/j.mser.2020.100604.
[56] H. Vahabi, B. Kandola, M. Saeb, Flame retardancy index for thermoplastic composites, Polymers (Basel) 11 (3) (2019) 407, https://doi.org/10.3390/polym11030407.
[57] W. Rao, P. Zhao, C. Yu, H.-B. Zhao, Y.-Z. Wang, High strength, low flammability, and smoke suppression for epoxy thermoset enabled by a low-loading phosphorus-nitrogen-silicon compound, Compos. Part. B-Eng. 211 (2021), 108640.
[58] Y. Zhang, W. Tian, L. Liu, W. Cheng, W. Wang, K.M. Liew, B. Wang, Y. Hu, Eco-friendly flame retardant and electromagnetic interference shielding cotton fabrics with multi-layered coatings, Chem. Eng. J. 372 (2019) 1077–1090.
[59] Y. Zhang, J. Yu, J. Lu, C. Zhu, D. Qi, Facile construction of 2D MXene ($Ti_3C_2T_x$) based aerogels with effective fire-resistance and electromagnetic interference shielding performance, J. Alloy. Comp. 870 (2021), 159442.
[60] F. Chu, X. Yu, Y. Hou, X. Mu, L. Song, W. Hu, A facile strategy to simultaneously improve the mechanical and fire safety properties of ramie fabric-reinforced unsaturated polyester resin composites, Compos. Part. A-Appl. S. 115 (2018) 264–273.
[61] F. Chu, C. Ma, T. Zhang, Z. Xu, X. Mu, W. Cai, X. Zhou, S. Ma, Y. Zhou, W. Hu, L. Song, Renewable vanillin-based flame retardant toughening agent with ultra-low phosphorus loading for the fabrication of high-performance epoxy thermoset, Compos. Part. B-Eng. 190 (2020), 107925.
[62] S. Dong, Y. Wang, A. Ashour, B. Han, J. Ou, Nano/micro-structures and mechanical properties of ultra-high performance concrete incorporating graphene with different lateral sizes, Compos. Part. A-Appl. S. 137 (2020), 106011.